Predicting the breaking strength of gravity water waves in deep and intermediate depth

MORTEZA DERAKHTI¹ † MICHAEL L. BANNER² and JAMES T. KIRBY³

¹Department of Civil Engineering, Johns Hopkins University, Baltimore, MD 21218, USA ²School of Mathematics and Statistics, The University of New South Wales Sydney, Sydney 2052 Australia

³ Center for Applied Coastal Research, Department of Civil and Environmental Engineerings, University of Delaware, Newark, DE 19716, USA

(Received?; revised?; accepted?.)

We revisit the classical but as yet unresolved problem of predicting the strength of 11 breaking 2-D and 3-D gravity water waves, as quantified by the amount of wave energy 12 dissipated per breaking event. Following Duncan (1983), the wave energy dissipation rate 13 per unit length of breaking crest may be related to the fifth moment of the wave speed and the non-dimensional breaking strength parameter b. We use a finite-volume Navier-Stokes solver with LES resolution and volume-of-fluid surface reconstruction (Derakhti & Kirby 2014a, 2016) to simulate nonlinear wave evolution, with a strong focus on breaking onset and post-breaking behavior for representative cases of wave packets with breaking due to dispersive focusing and to modulational instability. The present study uses these 19 results to investigate the relationship between the breaking strength parameter b and the breaking onset parameter B proposed recently by Barthelemy et al. (2018). The latter, formed from the local energy flux normalized by the local energy density and the local 22 crest speed, simplifies, on the wave surface, to the ratio of fluid speed to crest speed. Following a wave crest, when B exceeds a generic threshold value at the wave crest (Barthelemy et al. 2018), breaking is imminent. We find a robust relationship between the breaking strength parameter b and the rate of change of breaking onset parameter, dB/dt at the wave crest, as it transitions through the generic breaking onset threshold 27 $(B \sim 0.85)$, scaled by the local period of the breaking wave. This result significantly refines previous efforts to express b in terms of a wave packet steepness parameter, which is both difficult to define robustly and which does not provide a generically accurate forecast of the energy dissipated by breaking.

1. Introduction

37 38

10

We revisit the classical but as yet unresolved problem of predicting the breaking strength of 2-D and 3-D gravity water waves. The most commonly used approach is the Phillips (1985) spectral framework for the mean breaking crest length per unit area with speeds in the range $(\mathbf{c}, \mathbf{c} + d\mathbf{c})$. This is combined with the Duncan (1983) scaling argument for the wave energy dissipation rate per unit length of breaking crest, ϵ , given by

$$\epsilon = \frac{\tilde{\epsilon}}{\tau l} = b\rho g^{-1} c_b^5,\tag{1.1}$$

where $\tilde{\epsilon}$ is the total wave energy dissipation due to wave breaking, τ is the averaging period and is on the order of the active breaking period, l is the mean length of the

† Email address for correspondence: derakhti@jhu.edu

70

71

72

73

74

76

77

78

80

81

breaking crest during the averaging period, ρ is the density of the liquid phase, g is the gravitational acceleration, c_b is the phase speed of the breaking wave, and b is the dimensionless constant of proportionality, hereafter referred to as the breaking strength parameter.

Field and laboratory data have shown a strong dependence of b, within the scatter of 45 data, on the global wave steepness S calculated on the basis of spectral information for wave packets (Romero et al. 2012). Derakhti & Kirby (2016) provided a new scaling for b 47 based on the spectrally-averaged global steepness of a wave field, where the scatter of es-48 timates of b based on numerical computations was considerably decreased compared with 49 the existing formulations (Romero et al. 2012). The formulations of Romero et al. (2012) 50 and Derakhti & Kirby (2016) provide estimates of b > 0 for packets with S > 0.08. However, S for non-breaking packets can reach values of 0.3 or higher. Thus, another cri-52 terion, based on additional information beyond that provided by parameter S, is needed to distinguish between breaking and non-breaking packets. Also, although such a parameterization is adaptable via the spectral saturation for use in phase-averaged spectral wind-wave models, the evaluation of S is problematic in phase-resolved models. Finally, 56 we note that, existing versions of the data analysis (e.g., Banner & Peirson 2007) give 57 values of b for multiple-breaking events which fall appreciably below values reported for single-breaking focused wave packets (Romero et al. 2012, Figure 1), suggesting a significant physical difference between the mechanism of breaking in the two types of events. 60 However, this can be primarily attributed to different choices for averaging periods, as 61 discussed in detail in §4 below.

Barthelemy et al. (2018) showed that highest non-breaking waves were clearly separated from marginally breaking waves by their normalized energy fluxes localized near the crest tip region, and that initial breaking instability occurs within a very compact region centered on the wave crest. On the surface, the expression for normalized energy flux (denoted by symbol B) reduces to the ratio of fluid velocity at the crest to the translational velocity of the crest for the tallest wave in the evolving group. Barthelemy et al. (2018) found that a value of B=0.85 provides a robust threshold for breaking onset for 2-D wave packets propagating in deep or intermediate uniform water depths. Further targeted study of representative cases of the most severe laterally-focused 3-D wave packets in deep and intermediate depth water shows that the threshold remains robust. These numerical findings for 2-D and 3-D cases were closely supported by the observations of Saket et al. (2017, 2018).

Our goal here is to find a robust and local parameterization to predict the breaking strength of 2-D and 3-D gravity water waves. We use a large-eddy-simulation (LES)/volume-of-fluid (VOF) model (Derakhti & Kirby 2014a, 2016) to simulate nonlinear wave evolution, with a strong focus on breaking onset and post-breaking behavior for representative cases of wave packets, and examine breaking due to dispersive focusing and to modulational instability. Using these numerical results, we investigate the relationship between the breaking strength parameter b and the breaking onset parameter b proposed by Barthelemy b0 and the breaking onset parameter b1 proposed by Barthelemy b1. While the results are potentially applicable more generally, in this paper we concentrate on breaking events due to focusing or modulational instability in wave packets over flat bottom topography and for conditions ranging from deep to intermediate depth, with depth to wavelength ratios ranging from 0.68 to 0.13. Examination of depth-limited breaking or breaking due to strong opposing currents is left for future study.

Case	S	f_c	$\Delta f/f_c$	N	h	h/L_0	$\tan \theta(y)$	c_b	T_b	Γ	b
no.		(s^{-1})			(m)			(m/s)	(s)		$\times 10^{-3}$
A1	0.30	0.88	0.75	32	0.60	0.25	0	-	-	-	-
A2	0.3005	0.88	0.75	32	0.60	0.25	0	-	-	-	-
A3	0.302	0.88	0.75	32	0.60	0.25	0	1.71	1.14	0.45	0.4
A4	0.31	0.88	0.75	32	0.60	0.25	0	1.64	1.08	0.83	4.5
A5	0.41	0.88	0.75	32	0.60	0.25	0	1.59	1.04	1.22	30.1
A6	0.44	0.88	0.75	32	0.60	0.25	0	1.59	1.04	1.44	40.9
B1	0.25	0.88	0.75	32	0.25	0.13	[-0.8, 0.8]	1.35	1.30	1.29	45.1
B2	0.25	0.88	0.75	32	0.60	0.25	[-0.8, 0.8]	1.76	1.16	1.19	23.4
B3	0.35	0.88	0.75	32	0.60	0.25	[-0.5, 0.5]	1.68	1.06	1.62	72.7
B4	0.35	0.88	0.75	32	0.85	0.30	[-0.5, 0.5]	1.80	1.09	1.39	35.3
C1	0.32	0.75	1.0	32	0.60	0.17	0	1.94	1.41	0.65	1.6
C2	0.36	0.75	1.0	32	0.60	0.17	0	1.91	1.37	0.86	12.4
C3	0.40	0.75	1.0	32	0.60	0.17	0	1.95	1.43	1.14	22.3
M1	0.160	1.48	0.0954	2	0.55	0.68	0	0.88 - 0.92	0.56 - 0.59	0.61 - 1.07	1.4 - 16.9
M2	0.176	1.48	0.0954	2	0.55	0.68	0	0.89 - 0.95	0.57 - 0.61	0.46 - 1.12	0.3 - 17.3

Table 1. Input parameters for the simulated alongcrest-uniform (2-D) and short-crested (3-D) focused wave packets and 2-D modulated wave trains. x_f and t_f are 9 m and 20 s in 2-D and 5 m and 12 s in 3-D focused packets respectively.

2. Numerical experiments

100

101

103

104

106

107

A detailed description of the polydisperse two-fluid model and boundary conditions used may be found in Derakhti & Kirby (2014a, §2). Demonstrations of model convergence and performance may be found in Derakhti & Kirby (2014b, 2016). The model parameters for a polydisperse bubble phase are chosen as summarized in Derakhti & Kirby (2014a, Table 4). Here, the incident wave boundary condition and model set-up are discussed briefly.

We define the coordinate system (x, y, z) such that x and y represent the along-tank and transverse directions respectively and z is the vertical direction, positive upward and measured from the still water level. The reference time t^* and x-location x^* are taken as the time and location at which B following the crest tip reaches the threshold value of 0.85 for breaking packets, or its maximum for non-breaking packets, respectively and are normalized by the local period and wave length of the carrier wave respectively.

All model simulations are performed with the model initialized with quiescent conditions. An incident wave packet is then generated at the model upstream boundary. The input wave packet was composed of N sinusoidal components of steepness a_nk_n , $n=1,\cdots,N$ where $a_n=S/(Nk_n)$ and k_n are the amplitude and wave number of the nth frequency component and $S=\sum_{n=1}^N a_nk_n$ is the linear prediction of the wave packet global steepness. Based on linear theory, the free surface elevation for the 2-D (Rapp & Melville 1990; Derakhti & Kirby 2014a) and 3-D (Wu & Nepf 2002; Kirby & Derakhti 2018) focused packets at the wavemaker is given by

$$\eta(0, y, t) = \sum_{n=1}^{N} a_n \cos[2\pi f_n(t - t_f) + \frac{k_n x_f}{\cos \theta(y)}], \tag{2.1}$$

where f_n is the frequency of the *n*th component, x_f and t_f are the predefined, linear theory estimates of location and time of the focal point respectively, and $\theta(y)$ is the angle of incidence of each wave component at various transverse locations with $\cos \theta(y) = 1$

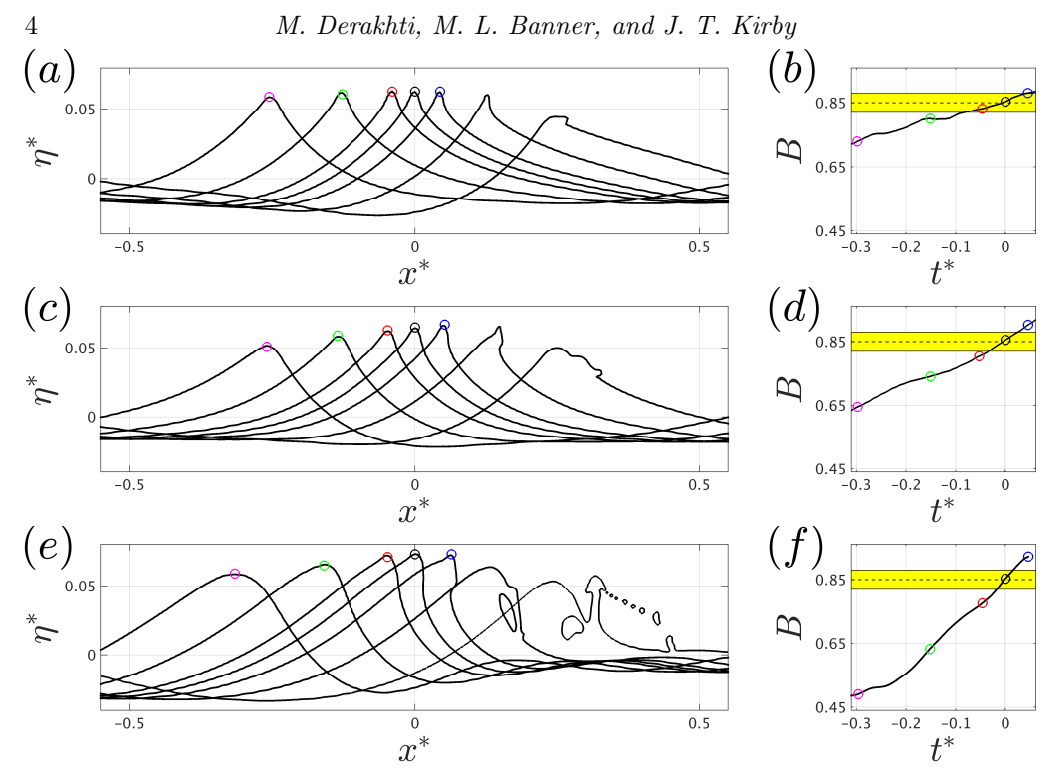


FIGURE 1. (a, c, e) Snapshots of the spatial variation of the normalized free surface elevations near the maximum crest, and (b, d, f) the temporal variation of B before and after the breaking onset for the weak spilling A3, spilling A4 and strong plunging A6 breaking 2-D focused packets.

in 2-D and $\cos \theta(y) = x_f / \sqrt{x_f^2 + y^2}$ in 3-D breaking cases. The discrete frequencies f_n were uniformly spaced over the band $\Delta f = f_N - f_1$ with a central frequency defined by $f_c = 1/2(f_N + f_1)$. Following the set up of the initially bimodal wave trains in Banner & Peirson (2007), the free surface elevation for a 2-D modulated wave train at the wavemaker is given by

$$\eta(0, y, t) = a_1 \cos(\omega_1 t) + a_2 \cos(\omega_2 t - \frac{\pi}{18}),$$
(2.2)

where $\omega_1 = 2\pi f_1$, $\omega_2 = \omega_1 + 2\pi \Delta f$, $S = a_1 k_1 + k_2 a_2$ and $a_2/a_1 = 0.3$. Increasing the global steepness S increases the strength of the resulting breaking event in both focused packets and modulated wave trains. Finally, fluid velocities for each component are calculated using linear theory and then superimposed at the wavemaker. Table 1 summarizes the input parameters for all simulated cases.

3. A new parameterization for the breaking strength parameter b

Figure 1 shows snapshots of free surface elevations before and after breaking onset as well as the temporal variation of B for the evolving wave crest for the single-breaking focused packets A3, A4 and A6. Figure 2 shows corresponding results for the multiple-breaking modulated wave train M2. Results show that, as the strength of breaking increases, the rate of change of B near the threshold value, $dB/dt|_{B_{th}}$, increases. Consistent with Barthelemy $et\ al.\ (2018)$, warning of imminent breaking onset ($t^*=0$ here) occurs up to a fifth of a carrier wave period prior to a breaking event. As a consequence, the wave form at $B=B_{th}$ is well defined and the free surface is single-valued.

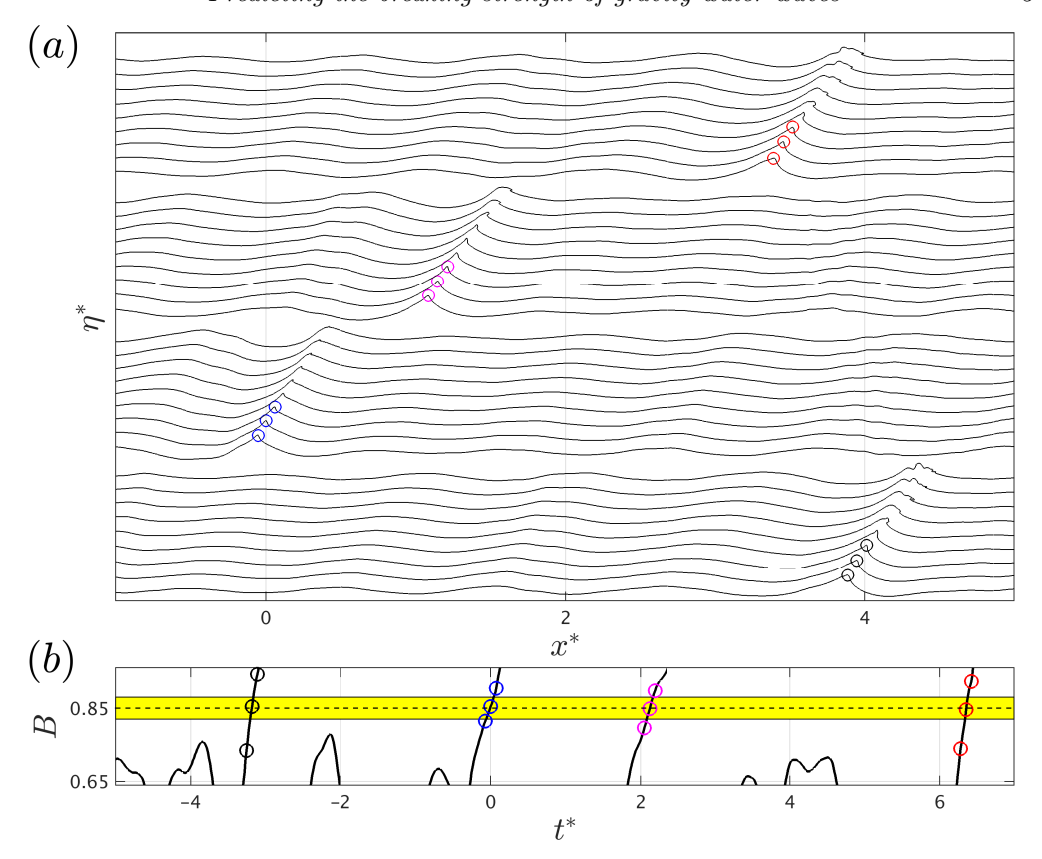


FIGURE 2. (a) Snapshots of the spatial variation of the normalized free surface elevations near the maximum crest, and (b) the temporal variation of B for four successive breaking events in the 2-D multiple-breaking modulated wave train M2.

132

133

134

135

136

138

139

140

142

143

144

145

146

147

148

Figure 3 shows a plan view of the spatial distribution of the normalized free surface elevations at $t^* = 0$ at which $B(y \sim 0) = B_{th}$ and after breaking onset at $t^* = 0.5$ as well as the spatio-temporal variation of B for the 3-D breaking focused packets B1, B2 and B4. The latter picture is constructed by displaying the corresponding B curves at each transverse location. In each case, the dashed lines in the left and middle columns of Figure 3 correspond to the two vertical dashed lines shown in the right column and show the location of the crest maximum at the associated times. Due to a strong 3-D focusing of the incident wave packet, the position of the crest maximum at each transverse location may experience rapid change even close to the breaking region, resulting in unrealistic dB/dt values. Panel (a) demonstrates an example of such a jump in the location of the maximum crest at $|y^*| \sim 0.6$. The corresponding high values of B shown in the panel (c) for $|y^*| \sim 0.6$ are then just an artifact of the post-processing method. Figure 3 also shows that the breaking process starts around $y^* = 0$, with the breaking crest gradually growing in width during the active breaking period, and that B has approximately the same temporal structure within the region close to the crest maximum location prior to breaking onset ($|y^*| < 0.15, -0.1 < t^*$). Further, the length of the breaking crest, as shown by the dotted-dashed line in the right column of Figure 3, expands proportional to $\sim (t-t_o)^{1/2}$ where t_o is the time at which the crest overturning starts. Such growth rate of the length of breaking crest is consistent with theoretical work of Pomeau et al.

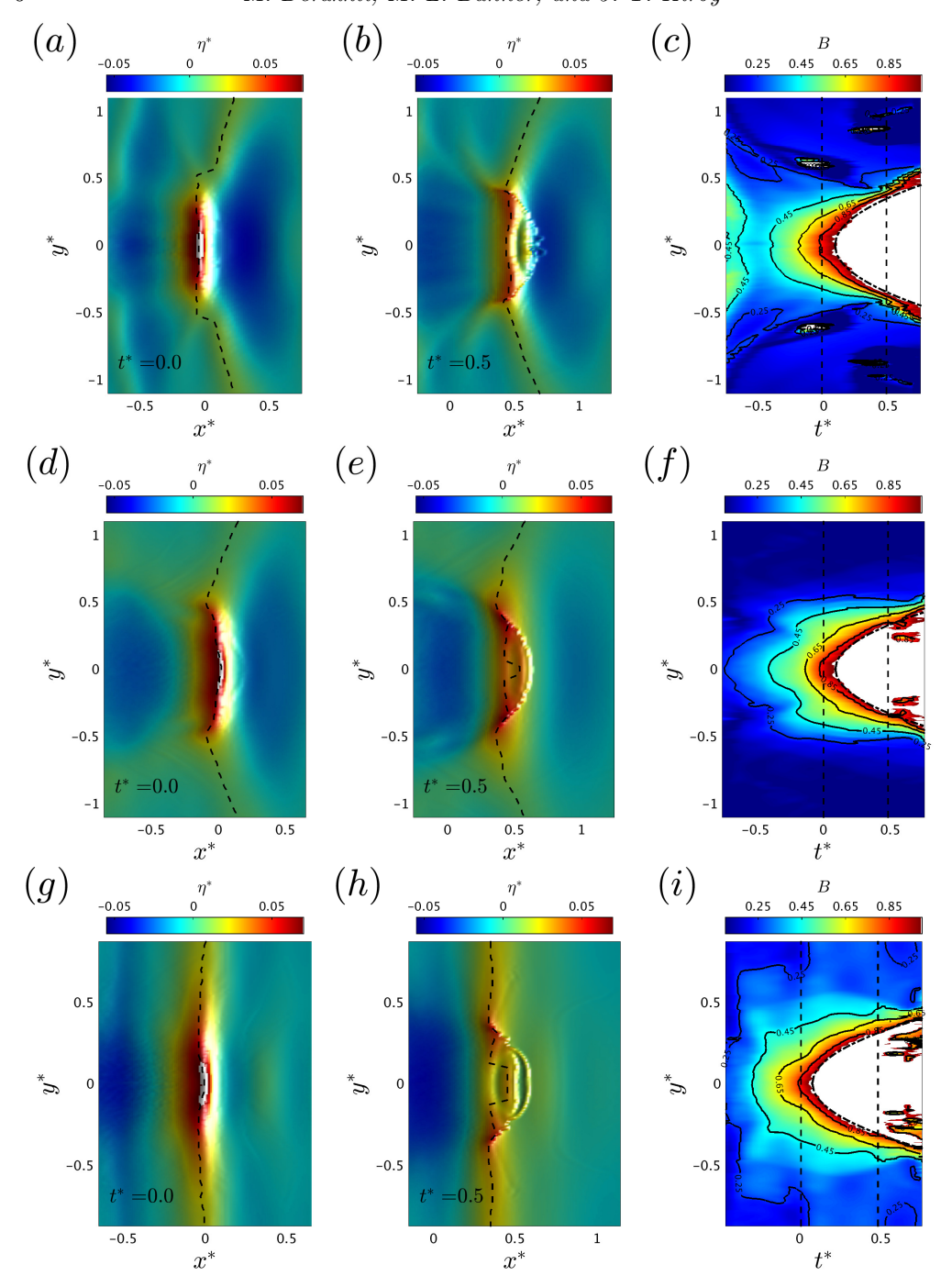


FIGURE 3. (Left and middle columns) Plan view of the spatial variation of the normalized free surface elevations near the maximum crest at (a,d,g) $t^*=0$, and (b,e,h) $t^*=0.5$, as well as (right column) the spatio-temporal variation of B for the 3-D focused packets (a,b,c) B1, (d,e,f) B2, and (g,h,i) B4. The corresponding crest locations of the two vertical dashed lines in the right frames are shown by the dashed lines in the left and middle frames in each case. In the right column, white color shows regions where B has exceeded a value of 1 or has become poorly defined due to breakdown of the smooth water surface. Dotted-dashed lines show $y^*=\pm\alpha_1(t^*-\alpha_2)^{1/2}$, where $\alpha_1\approx 0.5$ and $\alpha_2=0.09$.

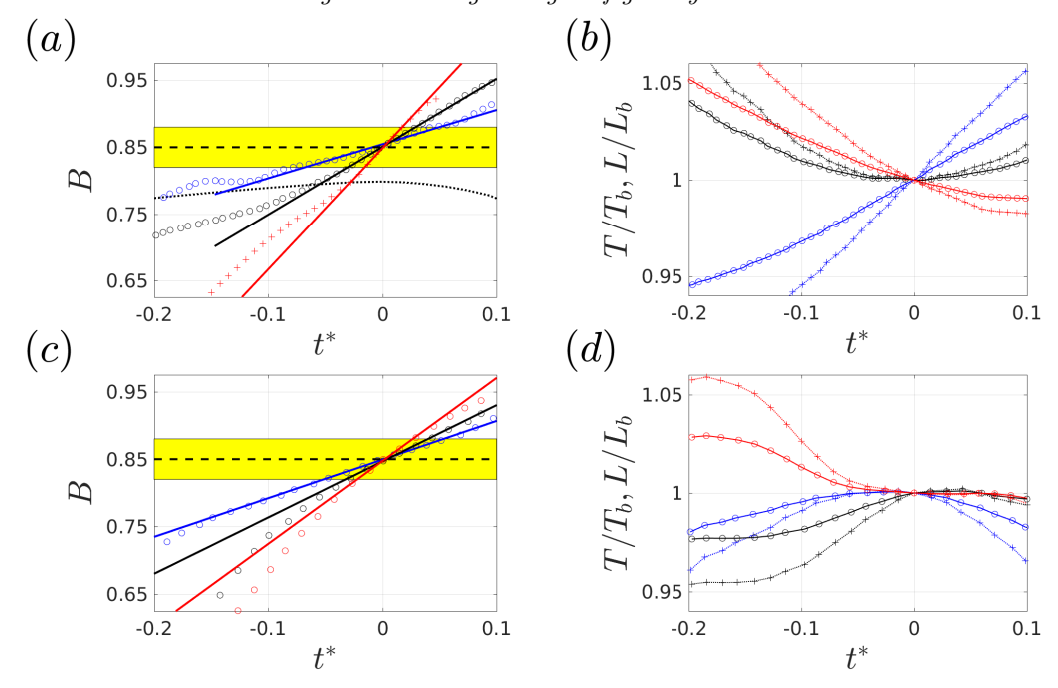


FIGURE 4. Temporal variation of (a, c) B, and (b, d) (dotted lines with markers) the local wave length L and (solid lines with markers) local wave period T, normalized by their corresponding values at $B = B_{th}$, for (a, b) various focused packets, and (c, d) three successive breaking events in modulated wave train M2. In (a) the dotted line represents the highly nonlinear non-breaking case A2. In (a, c), solid lines show the linear fit in the interval $|B - B_{th}| < 0.03$ shown by the yellow boxes. Here, L is defined by the two successive zero crossing points around the crest maximum (Figure 6), and T is obtained by using linear dispersion relation (Appendix A).

(2008). Hereafter we choose $B(y^* = 0)$ as the representative B value for the 3-D cases to compare with the 2-D cases for the proposed parameterization discussed below.

Panels (a) and (c) of Figure 4 present the temporal variation of B for a number of breaking events (with various breaking strengths) due to dispersive focusing and modulational instability, together with a highly nonlinear non-breaking case A2 which has a global steepness slightly smaller than the weakest breaking focused packet A3 (see Table 1). For breaking cases, a linear fit in the interval $|B-B_{th}| < \alpha$ ($\alpha = 0.03$ in Figure 4), shown by the yellow boxes, is also presented. The sensitivity of the results to choice of α will be examined below. The slope of each such fitted line, hereafter referred to as $dB/dt|_{B_{th}}$, will be used to parameterize the breaking strength parameter b.

To construct a non-dimensional parameter, we also need to identify an appropriate time scale, for which we choose the local period, T_b , of the carrier wave at $B = B_{th}$, obtained by using the linear dispersion relation and the local wave length L_b defined based on the two successive zero up- and zero down-crossing points around the crest maximum (see Figure 6). Panels (b) and (d) of Figure 4 show that estimates of L and T constructed in this manner have a small variation as the crest approaches breaking onset. Here, L_b and T_b refer to the associated values of L and T at $B = B_{th}$ respectively.

Figure 5 shows the variation of the breaking strength parameter b with the new parameter $\Gamma = T_b dB/dt|_{B_{th}}$ for all simulated cases. Our methodology to calculate the breaking strength parameter b is similar to that used in Derakhti & Kirby (2016) with a modification explained in the Appendix A. The reader is referred to Derakhti & Kirby (2014a,b,

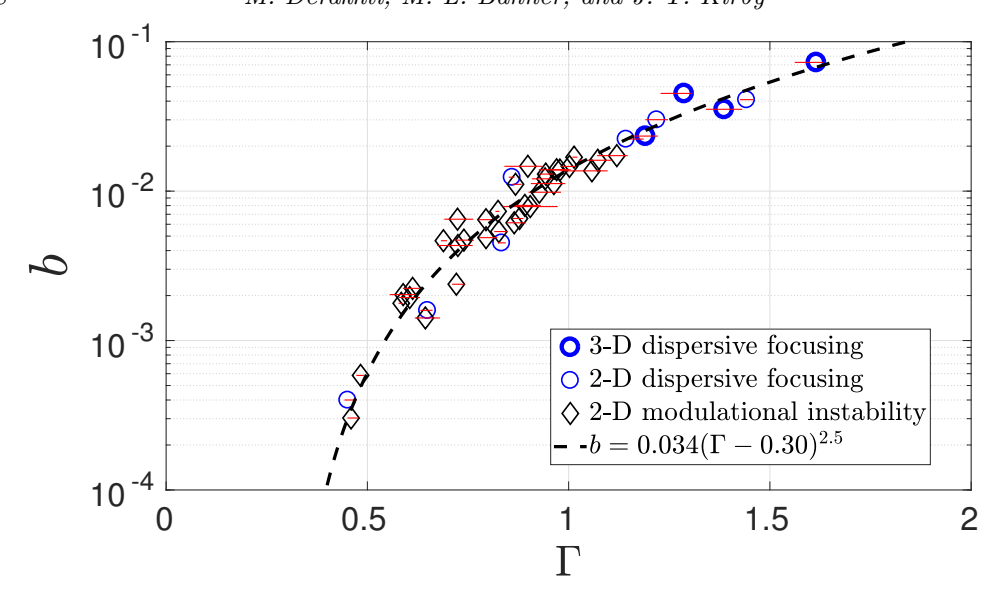


FIGURE 5. Variation in the breaking strength parameter b with the new parameter $\Gamma = T_b dB/dt|_{B_{th}}$ that represents the normalized rate of change of B as it transitions through the breaking onset. Dashed line indicates a fitted curve to the numerical data. Red line segments represent sensitivity to choice of α in the estimation of dB/dt obtained by linear curve fitting in the interval $|B - B_{th}| < \alpha$.

2016) for the detailed examination of the model prediction of the total energy dissipation compared with corresponding measured data, as well as the sensitivity of the simulation results with respect to the selected grid resolution. In summary, we found that model estimates of the loss of total wave energy due to wave breaking are typically within 10% of observed levels, after correcting for the change in the downstream group velocity following breaking (Derakhti & Kirby 2016). As a result, the uncertainty in the predicted b values are expected to be less than 10% for the cases considered here.

For each case, the horizontal red line segment in Figure 5 shows the variation of Γ with respect to the selected interval $|B - B_{th}| < \alpha$, (with $0.02 \le \alpha \le 0.05$), to perform the linear fit to obtain $dB/dt|_{B_{th}}$, and the marker represents the associated averaged value of Γ . Results show that the rate of change of B following the crest tip as it transitions through the breaking onset, and thus the parameter Γ , are not sensitive to a specific choice of α for $\alpha \le 0.05$. Finally, the results show that Γ can successfully predict the breaking strength parameter b. Assuming a formulation with the form $b \sim a_1(\Gamma - a_2)^{a_3}$ and using the least-square curve fitting technique, we obtain

$$b = 0.034(\Gamma - 0.30)^{2.5}. (3.1)$$

4. Discussion and Conclusions

The results shown in Figure 5 establish that the strength of individual breaking events in an irregular wave train, as well as the onset of breaking, can be estimated from properties of the wave crest as it approaches breaking. This is the centerpiece figure of this paper, and shows a systematic collapse of the proposed breaking strength predictor Γ for a diverse range of representative 2-D water wave focused packets and modulated wave trains in deep and intermediate depth waters, as well as several cases of 3-D dispersive focusing packets.

A significant finding is that the results in Figure 5 do not show a pronounced difference between values of b obtained for focused packets or modulational events. This result contrasts with previous discussions of the two cases (e.g., Romero $et\ al.\ 2012$, Figure 1) where reported b values for modulational cases appear to be significantly smaller than values for focused packet breaking events. This discrepancy results from different choices of averaging procedures between investigators in the analysis of data for wave packets (usually on the order of the local carrier wave period T_b) and modulated wave trains (usually on the order of the wave group period T_g); in our modulated wave trains (Figure 2) have considerably different breaking events in our modulated wave for the modulational cases in Figure 5 represent b for each successive breaking event, as opposed to an average over multiple events within a group (e.g., Banner & Peirson 2007; Allis 2013). For example, we find that b varies in the range 0.3×10^{-3} to 17.3×10^{-3} for the case M2 with an ensemble value of $\sim 6 \times 10^{-3}$. A recent comparison of this aspect of the b methodology is shown in Derakhti & Kirby (2016, Figure 14).

Based on these findings, we conclude that there is no significant difference between the mechanics of breaking events in focused or modulated wave trains, in contrast to previous discussions based on inconsistent methods for estimating b. This conclusion is strongly supported by the different sets of published b measurements. These show that the dynamic range of reported b values, from weak to strong breaking, is very similar for focused and modulation-induced breaking cases within each data set, based on the b estimation methodology utilized.

The success of the parameterization for predicting breaking strength found here would make it possible to better describe breaking events in codes based on potential flow theory, such as high-order spectral (HOS) codes, where breaking is not predicted by the model itself (see Ducrozet et al. 2017, for a recent review of the HOS approach). The development of criteria for the onset and strength of breaking in such models has long been a subject for investigation. Recently, Seiffert et al. (2017) have investigated the use of the parameter B as a breaking onset criterion in HOS, while Seiffert & Ducrozet (2018) discuss the specification of an eddy viscosity model after the onset of breaking is identified. It is our belief that the specification of such a dissipation model should be based on the parameterization of total dissipation in terms of the rate of change of B developed here, which would provide a strong link between the present work and operational wave modeling.

The universality of the B parameter and its rate of change as robust indicators of wave breaking onset and strength clearly warrant further study. We close by reiterating that the present work provides a first indication of a direct link between the local properties of a wave crest as it transitions through an apparently generic breaking threshold, and the resultant overall energy dissipation resulting from the breaking event. The results are underpinned by fundamental energy flux considerations as proposed in Barthelemy et al. (2018).

Acknowledgments: This work was supported by the National Science Foundation, Physical Oceanography Program grants OCE-1435147, OCE-1756040 and OCE-1756355, and through the use of computational resources provided by Information Technologies at the University of Delaware. M.B. also gratefully acknowledges support from the Australian Research Council for his breaking waves research. The LES/VOF code is based on the model code TRUCHAS, provided by the Los Alamos National Laboratory, Department of Energy.

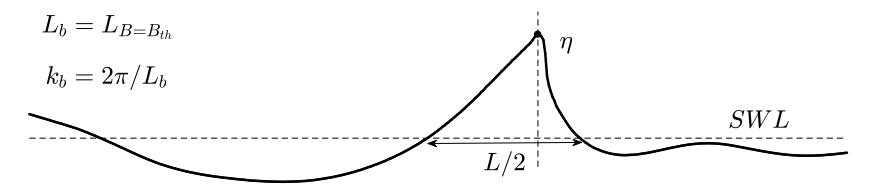


FIGURE 6. Definitions of the local wave parameters. L is the local wave length, L_b is the associated value of L at breaking onset at which $B = B_{th} = 0.85$, and $k_b = 2\pi/L_b$ is the local wave number at breaking onset.

Appendix A. Determination of the breaking strength parameter b

Rearranging (1.1), the breaking strength parameter b is written as

$$b = \frac{g\tilde{\epsilon}}{\rho c_b^5 \tau l},\tag{A1}$$

where $\tilde{\epsilon}$ is the total wave energy dissipation due to wave breaking, $\tau \sim O(T_b)$ is the averaging period and is usually on the order of the active breaking period, and l is mean length of the breaking crest during the active breaking period, $0 < t - t_b < \tau$. Following Derakhti & Kirby (2016) and Tian et al. (2008), we estimate the local wavenumber at breaking onset, k_b , defined based on the two successive zero up- and zero down-crossing points around the crest maximum as shown in Figure 6. Then, the linear dispersion relation is used to estimate the breaking wave phase speed and period as $c_b = (g/k_b \tanh k_b h)^{1/2}$ and $T_b = 2\pi/k_b c_b$ respectively.

As described by Derakhti & Kirby (2014a, §4.3), the dissipation rate during active breaking has a strong spatio-temporal variation, and thus $\epsilon = \tilde{\epsilon}/\tau l$ may be interpreted as an averaged dissipation rate in the interval $0 < t - t_b < \tau$. Following Derakhti & Kirby (2014a, 2016), we set $\tau = 0.75T_b$.

Derakhti & Kirby (2016) describe a methodology for computing $\tilde{\epsilon}$ in focused wave packet experiments that depends on the spatial isolation of breaking events and on the fact that the domain is essentially quiescent before and after passage of the wave train. For multiple-breaking cases, and, particularly for the modulational instability cases considered here, the spatial extent of breaking events may overlap in time, rendering the integral-over-all-time approach described by Derakhti & Kirby (2016) inapplicable. A modification to allow for localization of the total energy loss estimate in both space and time is described here. Starting from a local equation for mechanical energy e(x,y,z,t) and energy flux $\mathbf{f} = \mathbf{u}(p+e)$ per unit volume,

$$e_{,t} + \nabla \cdot \mathbf{f} = \epsilon' \tag{A2}$$

where ϵ' represents dissipation/unit volume, we consider the breaking event to be isolated within a region $x_1 \leqslant x \leqslant x_2, y_1 \leqslant y \leqslant y_2, t_1 \leqslant t \leqslant t_2$. Integrating (A 2) over depth and then over x, y and t gives

$$\left[\int_{x_{1}}^{x_{2}} \int_{y_{1}}^{y_{2}} \int_{-h}^{\eta} e \, dz \, dy \, dx \right]_{t_{1}}^{t_{2}} + \left[\int_{y_{1}}^{y_{2}} \int_{t_{1}}^{t_{2}} \int_{-h}^{\eta} f_{x} \, dz \, dt \, dy \right]_{x_{1}}^{x_{2}} + \left[\int_{x_{1}}^{x_{2}} \int_{t_{1}}^{t_{2}} \int_{-h}^{\eta} f_{y} \, dz \, dt \, dx \right]_{y_{1}}^{y_{2}} =$$

$$= \int_{x_{1}}^{x_{2}} \int_{y_{1}}^{y_{2}} \int_{t_{1}}^{t_{2}} \int_{-h}^{\eta} \epsilon' dt \, dz \, dy \, dx = \tilde{\epsilon}, \tag{A 3}$$

where $t_1 \leq t_b$ and $\tau \ll t_2 - t_b$, where t_b is the time of breaking onset as defined in §2.

REFERENCES

- ALLIS, M. J. 2013 The speed, breaking onset and energy dissipation of 3d deep-water waves. PhD thesis, U. New South Wales.
- 271 BANNER, M. L. & PEIRSON, W. L. 2007 Wave breaking onset and strength for two-dimensional deep-water wave groups. *Journal of Fluid Mechanics* 585, 93–115.
- BARTHELEMY, X., BANNER, M. L., PEIRSON, W. L., FEDELE, F., ALLIS, M. & DIAS, F. 2018
 On a unified breaking onset threshold for gravity waves in deep and intermediate depth
 water. Journal of Fluid Mechanics 841, 463–488.
- DERAKHTI, M. & KIRBY, J. T. 2014a Bubble entrainment and liquid bubble interaction under unsteady breaking waves. J. Fluid Mech. 761, 464–506.
- Derakhti, M. & Kirby, J. T. 2014b Bubble entrainment and liquid bubble interaction under unsteady breaking waves. Research Report CACR-14-06. Center for Applied Coastal Research, University of Delaware, available at http://www.udel.edu/kirby/papers/derakhti-kirby-cacr-14-06.pdf.
- Derakhti, M. & Kirby, J. T. 2016 Breaking-onset, energy and momentum flux in unsteady focused wave packets. *Journal of Fluid Mechanics* **790**, 553–581.
- Ducrozet, G., Bonnefoy, F. & Perignon, Y. 2017 Applicability and limitations of highly non-linear potential flow solvers in the context of water waves. *Ocean Engineering* **142**, 233–244.
- Duncan, J. H. 1983 The breaking and non-breaking wave resistance of a two-dimensional hydrofoil. J. Fluid Mech. 126, 507–520.
- Kirby, J. T. & Derakhti, M. 2018 Short-crested wave breaking. European Journal of Mechanics/B Fluids in press.
- PHILLIPS, O. M. 1985 Spectral and statistical properties of the equilibrium range in windgenerated gravity waves. J. Fluid Mech. 156, 505–31.
- Pomeau, Y., Le Berre, M., Guyenne, P. & Grilli, S. 2008 Wave-breaking and generic singularities of nonlinear hyperbolic equations. *Nonlinearity* **21** (5), T61.
- RAPP, R. J. & MELVILLE, W. K. 1990 Laboratory measurements of deep-water breaking waves.
 Philosophical Transactions of the Royal Society A 331, 735–800.
- ROMERO, L., MELVILLE, W. K. & KLEISS, J. M. 2012 Spectral energy dissipation due to surface wave breaking. J. Phys. Oceanography 42, 1421–1444.
- SAKET, A., PEIRSON, W. L., BANNER, M. L. & ALLIS, M. J. 2018 On the influence of wave breaking on the height limits of two-dimensional wave groups propagating in uniform intermediate depth water. *Coastal Eng.* **133**, 159–165.
- Saket, A., Peirson, W. L., Banner, M. L., Barthelemy, X. & Allis, M. J. 2017 On the threshold for wave breaking of two-dimensional deep water wave groups in the absence and presence of wind. *J. Fluid Mech.* 811, 642–658.
- SEIFFERT, B. R. & DUCROZET, G. 2018 Simulation of breaking waves using the high-order spectral method with laboratory experiments: wave-breaking energy dissipation. *Ocean Dynamics* **68**, 65–89.
- SEIFFERT, B. R., DUCROZET, G. & BONNEFOY, F. 2017 Simulation of breaking waves using the high-order spectral method with laboratory experiments: wave-breaking onset. *Ocean Modelling* 119, 94–104.
- Tian, Z., Perlin, M. & Choi, W. 2008 Evaluation of a deep-water wave breaking criterion.

 Phys. Fluids 20, 066604.
- Wu, C. H. & Nepf, H. M. 2002 Breaking criteria and energy losses for three-dimensional wave breaking. *Journal of Geophysical Research* **107** (C10), 3177.